Mapping electromagnetic dualities via quantum decoherence measurements in 2D materials

J. J. Heremans[a], Yuantao Xie[a], S. L. Ren[a], C. Le Priol[b], and M. B. Santos[c]

[a]Physics Department, Virginia Tech, Blacksburg, VA 24061, USA
[b]Physics Department, Ecole Polytechnique, 91128 Palaiseau, France
[c]Homer L. Dodge Department of Physics and Astronomy, University of Oklahoma, Norman, OK 73019, USA

ABSTRACT

The quantification of quantum phase coherence can reveal several properties of charge carriers in systems of given dimensionality, illuminating mechanisms leading to quantum decoherence due to inelastic scattering events, to decoherence mechanisms due to device geometry, and to dephasing due to geometrical phases from applied fields. Examples of several effects are presented. Quantum phase coherence lengths were measured in mesoscopic geometries by quantum transport methods including universal conductance fluctuations, weak-localization, and quantum interferometry. The geometries were fabricated from two-dimensional starting materials. In wires of materials with strong spin-orbit interaction, we show that spin decoherence due to spin-orbit interaction and dephasing due to applied magnetic fields show an electromagnetic duality. We show that dephasing due to applied magnetic fields can be expressed in terms of a magnetic length quantifying time-reversal symmetry breaking. In wires, the main orbital quantum decoherence mechanism related to the wire length appears as environmental coupling decoherence, with longer wires showing asymptotically longer phase coherence lengths. For mesoscopic stadia, the geometry plays an additional role, inducing stadium-wire coupling decoherence.

Keywords: quantum coherence, mesoscopic physics, spin-orbit interaction, quantum wire, weak-localization, universal conductance fluctuations

Address all correspondence to: Jean J. Heremans, Virginia Polytechnic Institute and State University, Department of Physics, 850 West Campus Drive, Blacksburg, VA 24061, Tel: 1 540-231-4604; E-mail:heremans@vt.edu

1. INTRODUCTION

The rise of quantum information processing and quantum technologies lend new importance to the understanding of quantum phase decoherence. Important parameters in this respect are the electrons' quantum phase coherence length L_ϕ (defined as the length scale over which quantum coherence is maintained when the system is considered spinless), and the spin coherence length L_S. In mesoscopic systems, the quantum phases of carrier states can be randomized by inelastic or quasi-elastic processes dependent on temperature T, such as electron-phonon and electron-electron scattering[1–3] and energy

level broadening exceeding the Thouless energy.[4] Decoherence can also be caused by mechanisms without T-dependence, such as environmental coupling decoherence[5,6] due to connecting quantum systems to classical environments. Environmental coupling decoherence is often expressed using an escape rate $1/\tau_d$, where the dwell time τ_d is proportional to system size and limits the quantum phase coherence time τ_ϕ at low T.[7] Here $L_\phi = \sqrt{D\tau_\phi}$, where D denotes the carrier diffusion coefficient. In this work we describe how in addition to decoherence mechanisms, dephasing by geometrical quantum phases can also reduce apparent quantum coherence (decoherence is irreversible, while dephasing is reversible[8]). The two contributions blend in actual experiments. Dephasing by geometrical quantum phases contains information about fundamental physics phenomena. To extract this information however, it is necessary to quantify sources of decoherence. In this work, mesoscopic wires were studied, fabricated on InGaAs/InAlAs and InSb/InAlSb heterostructures harboring two-dimensional electron systems (2DESs). Also studied were wires fabricated on thin film Bi and mesoscopic stadia with side-wires fabricated on InGaAs/InAlAs heterostructures. Few previous investigations studied the effects of device-device coupling on decoherence between devices of different geometries, and here we describe a notable influence of *stadium-wire* coupling in the stadia with side-wires. The experiments use quantum interference effects in electronic transport, namely weak-antilocalization (WAL)[9–13] and universal conductance fluctuations (UCFs),[1,14–16] to measure L_ϕ. Since in the wires WAL dominates over UCFs, and *vv* for stadia, WAL is used to extract L_ϕ in the wires and UCFs are used in the stadia. Measurements were obtained by four-contact techniques under low constant-current excitation in a ^{3}He cryostat, over variable T from 0.38 K to 5.0 K. The low T leads to sufficiently long L_ϕ to study quantum interference phenomena,[4,17] and brings out decoherence mechanisms weakly dependent on T.

2. EXPERIMENTAL ASPECTS

The mesoscopic geometries studied in this work consisted of wires and stadia (wide 2D quantum dots). Parent materials to fabricate the mesoscopic devices were Bi(111) thin films (rhombohedral notation),[16,18] an InSb/In$_{0.85}$Al$_{0.15}$Sb heterostructure,[19] a high-mobility In$_{0.64}$Ga$_{0.36}$As/In$_{0.45}$Al$_{0.55}$As heterostructure,[4,17] and an In$_{0.53}$Ga$_{0.47}$As/In$_{0.52}$Al$_{0.48}$As lattice-matched bottom-doped heterostructure.[20] The devices were defined by electron-beam lithography and wet and reactive ion etching. Figure 1 depicts scanning electron micrographs of example geometries defined on the In$_{0.53}$Ga$_{0.47}$As/In$_{0.52}$Al$_{0.48}$As heterostructure, and conveys the dimensions of the devices as discussed below. Bi(111) thin films were thermally evaporated from 99.999% Bi sources on a SiO$_2$ (oxidized Si(001)) substrate,[16,18] to a thickness of 75 nm. The films show an orientation with the trigonal axis perpendicular to the substrate with grains of size 200-500 nm randomly oriented. The film surface is hence the trigonal face (Bi(111) in rhombohedral notation). The surface carriers on Bi(111)[21] dominate the transport properties with particularly a central electron pocket (along the trigonal axis) with effective mass $\sim 0.5\, m_e$ with m_e the free electron mass) determining the quantum transport measurements. As expected for high-quality semimetallic Bi, multicarrier fits to the magnetotransport data show compensated electron and hole densities $\sim 2\text{x}10^{24}\,\text{m}^{-3}$ and show mobilities $\sim 0.1\,\text{m}^2/\text{Vs}$. Wires on Bi had a length $L = 16$ µm and varying widths W. The In$_{0.85}$Al$_{0.15}$Sb/InSb/In$_{0.85}$Al$_{0.15}$Sb heterostructure, grown by molecular beam epitaxy (MBE) on (001) GaAs substrate, housed an InSb quantum well of thickness 25 nm[19] in which the 2DES is located. At $T = 0.39$ K the unpatterned 2DES had areal electron density $N_S = 5.2\text{x}10^{15}\,\text{m}^{-2}$ with mobility $\mu = 9.7\,\text{m}^2/\text{Vs}$, yielding a mean-free-path $\ell_e \approx 3.3$ µm. Here $\ell_e = v_F\tau_e$ where τ_e is the momentum scattering time and v_F the Fermi velocity. Wires on the InSb 2DES had $L = 24$ µm and varying W. The high-mobility In$_{0.64}$Ga$_{0.36}$As/In$_{0.45}$Al$_{0.55}$As heterostructure[4,17] was obtained by MBE
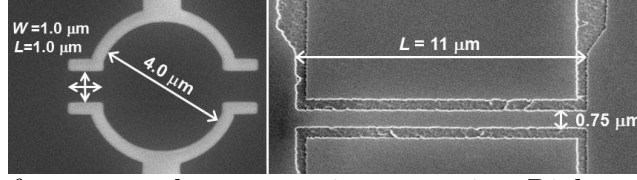
Figure 1: Micrographs of two example mesoscopic geometries. Right panel: an example stadium sample with side-wires with $W = 1$ µm and $L = 1$ µm. Etched trenches, which form barriers confining the electrons, appear as lighter regions. Left panel: two U-shaped trenches define a wire between them, here with length $L = 11$ µm

on (001) GaAs substrate, and housed an $In_{0.64}Ga_{0.36}As$ quantum well of thickness 10 nm, with at $T = 0.39$ K unpatterned 2DES density $N_S = 1.1 \times 10^{16}$ m^{-2} with $\mu = 4.7$ m^2/Vs and $\ell_e \approx 1.5$ µm. Wires on the InSb 2DES had $L = 24$ µm and varying W. The $In_{0.53}Ga_{0.47}As/In_{0.52}Al_{0.48}As$ heterostructure[20] was bottom-doped to obtain asymmetry in the quantum well confinement potential and hence strong spin-orbit interaction (SOI). The heterostructure was grown by MBE on InP(001) substrate, with a 10 nm wide $In_{0.53}Ga_{0.47}As$ quantum well. The 2DES showed $N_S = 2.02 \times 10^{16}$ m^{-2} and $\mu = 1.49$ m^2/(Vs) at $T = 0.38$ K, with $\ell_e = 0.77$ µm. Wires with $L = 2.0$ µm, 4.0 µm, 6.0 µm and 11.0 µm and with lithographic width 0.75 µm, as well as stadia with constant inner diameter 4.0 µm, and with varying wire-like necks (for dimensions, *cfr* Fig. 1) were patterned on this heterostructure. For all materials, transport properties stayed appreciably constant over the range of T in the measurements. Starting from the 2D parent materials, the wires on the heterostructures operate in the quasi-one-dimensional (Q1D) regime, meaning that the Fermi wavelengths $\lambda_F \ll W$ such that quantization in transverse subbands can be neglected, and that both $L_\phi > W$ and $\ell_e > W$.

3. MODELS FOR QUANTUM TRANSPORT

The data used to extract values for L_ϕ consists of device conductance G as function of magnetic field B applied normally to the 2D material. The data display the characteristic shape of WAL, where the magnetoconductance $G(B)$ drops sharply as $|B|$ is increased from zero, and UCFs[16] are also prominent. An example of measured $G(B)$ *vs* B with strong UCFs and the characteristic WAL negative magnetoconductance at low B, is contained in Fig. 2 for a stadium with side-wires of dimensions $W = 1.4$ µm and $L = 1.0$ µm (Fig. 1). We describe the models fitted to the measured $G(B)$ to extract values of L_S (by WAL analysis) and L_ϕ (by WAL or UCF analysis). The parent materials possess substantial SOI and are non-magnetic, and hence L_S is here limited by spin decoherence originating in SOI. WAL results from quantum interference of time-reversed trajectories of a diffusing electron returning to its starting point. Under SOI, singlet and triplet contributions arise from the pairs of time-reversed trajectories. In 1D, the quantum correction to conductance $\delta G(B)$ due to each contribution scales as an effective coherence length and the combination of the lengths amounts to the 1D WAL correction[9, 10, 22, 23]

$$\delta G(B) = -\frac{1}{2}\frac{e^2}{\pi\hbar}\frac{1}{L}(L_{1,1} + L_{1,-1} + L_{1,0} - L_{0,0}) \tag{1}$$

where $L_{0,0} = \left(L_\phi^{-2} + L_B^{-2}\right)^{-\frac{1}{2}}$ is the effective length for the singlet, and $L_{1,\pm 1} = \left(L_\phi^{-2} + L_S^{-2} + L_B^{-2}\right)^{-\frac{1}{2}}$ and $L_{1,0} = \left(L_\phi^{-2} + 2L_S^{-2} + L_B^{-2}\right)^{-\frac{1}{2}}$ are effective lengths for the triplets. In laterally unconfined 2D
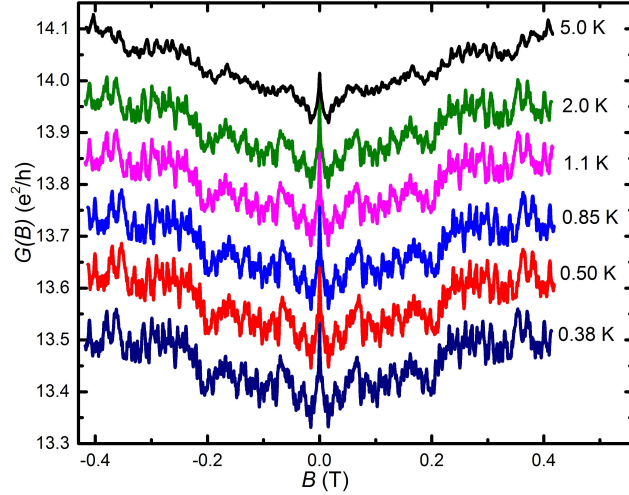
Figure 2: Magnetoconductance data $G(B)$ *vs* B for a stadium with side-wires with $W = 1.4$ µm and $L = 1.0$ µm, plotted over variable T. The amplitude of the UCFs decreases with increasing T due to the expected decrease in L_ϕ with increasing T. The dominant UCF signature was used in the stadia samples to obtain L_ϕ.

or 3D systems, the magnetic length $L_B = l_m \equiv \sqrt{\hbar/eB}$. In narrow wires in the ballistic transport regime with $\ell_e \gtrsim 0.6\,W$ and at low B limited by $l_m > \sqrt{W\ell_e}$, an expression accounting for flux cancellation[17,24] is used, $L_B = l_m\sqrt{C_1 l_m^2 \ell_e/W^3}$. In the ballistic regime and at intermediate B such that $W < l_m < \sqrt{W\ell_e}$, the crossover expression[9,10,17,24] is used, $L_B = l_m\sqrt{C_1 l_m^2 \ell_e/W^3 + C_2\ell_e^2/W^2}$. Here $C_1 = 4.75$ and $C_2 = 2.4$ for specular boundary scattering adopted in the samples here due to the existence of depletion layers at edges.[9,10,24]

UCFs in $G(B)$ are analyzed using a correlation function to bring out quantum coherence effects dependent on L_ϕ. The correlation function is defined[8] as $\overline{\delta G(B)\delta G(B + \Delta B)} = \langle[G(B) - \langle G(B)\rangle][G(B + \Delta B) - \langle G(B)\rangle]\rangle$, where angled brackets denote an average over a range of B. Taking $B_\phi = \hbar/(4eL_\phi^2)$ as the B under which one flux quantum h/e threads the area $8\pi L_\phi^2$, if $B >> B_\phi$ the following expression allows determination of L_ϕ:

$$\overline{\delta G(B)\delta G(B + \Delta B)} = \overline{\delta G^2(B)}\frac{1}{b}\Psi'(\frac{1}{2} + \frac{1}{b}) \tag{2}$$

with $\Psi(x)$ the digamma function and $b = \Delta B/2B_\phi$.

4. ANALYSIS OF GEOMETRICAL PHASE EFFECTS

Figure 3 shows values of L_S obtained using WAL analysis at $T = 0.39$ K on InSb and Bi wires, *vs* wire width W.[9,16] It is apparent that L_S increases with decreasing W, and in fact $L_S \sim 1/W$. In unconfined 2D systems, we have $L_S = L_\Omega$ for Rashba SOI,[25] assuming the D'yakanov-Perel motional narrowing spin decoherence is dominant. Here the spin precession length $L_\Omega = v_F/\Omega$ with Ω the spin precession frequency from the effective magnetic field arising from SOI. The unconfined spin decoherence rate is then expressed as $1/\tau_S = \Omega^2\tau_e/2$.[26] With $L_S = \sqrt{D\tau_S}$, where D is the diffusion coefficient, we
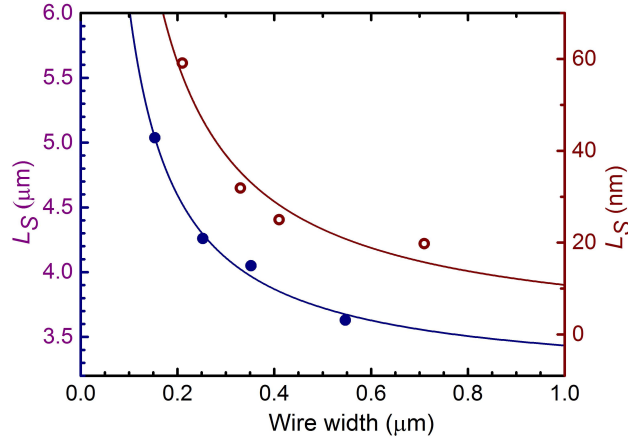
Figure 3: Values for L_S obtained by WAL analysis *vs* wire width (W). For InSb wires navy-colored filled symbols are used (left vertical axis) and for Bi wires brown open symbols are used (right vertical axis). Solid lines represent fits to a relation $L_S \propto 1/W$.

indeed have $L_S = L_\Omega$. Yet, in wires it is predicted[26] that $L_S = \sqrt{12}L_\Omega^2/W$, consistent with Fig. 3. This expression maps onto the behavior of L_B in wires,[17,24] where the expressions above for L_B denote a dependence on W such that L_B increases when W narrows. In fact in the non-ballistic case, boundary conditions for a wire yield $L_B = \sqrt{3}\,l_m^2/W$, emphasizing the similar function of L_Ω under SOI and the magnetic l_m under B. The data in Fig. 3 are hence consistent with an electromagnetic mapping between phenomena under SOI and under applied B. The role played by L_B in decoherence phenomena is illustrated by the singlet length $L_{0,0} = \left(L_\phi^{-2} + L_B^{-2}\right)^{-\frac{1}{2}}$, where L_B and L_ϕ have identical influence in limiting quantum coherence effects in Eq. (1). The triplet lengths illustrate that L_S likewise assumes this influence in limiting quantum coherence, albeit in a more complicated way due to the specific nature of spin. We now investigate why B, via L_B, contributes to an effective decoherence. Quantum interference between partial waves in B experience an Aharonov-Bohm (AB) geometrical quantum phase[3,4,17,27] dependent on their path in real space. Time-reversed paths will accumulate opposite AB phases, the mechanism whereby B breaks time-reversal symmetry. The magnetic length l_m (unconfined) or L_B (confined) serves as the characteristic length over which time-reversed partial waves dephase in B due to their relative accumulated AB phases. A unity quantum AB phase is accumulated in an unconfined system over a closed loop if the loop encloses a magnetic flux $\hbar/e$. Denoting the area enclosed by the loop as L_B^2, it is found that $L_B = l_m \equiv \sqrt{\hbar/(eB)}$. As noted above, $L_B = \sqrt{\hbar/(eB)}$ only applies to unconfined systems, while the above other expressions for L_B have been specifically derived to apply to confined and ballistic systems. Yet in general the characteristic length for breaking of time-reversal symmetry by dephasing, is L_B and for this reason L_B has a role equivalent to L_ϕ in expressions of decoherence. It is not surprising that the accumulation of an AB phase can be expressed in terms of a length scale L_B, because the AB quantum phase is an example of a geometrical phase. This fact also delivers insight in the expression $L_B = \sqrt{3}\,l_m^2/W$. If the closed loop is constrained to have dimension $W < l_m$ in one direction, the electron can acquire the same AB phase by traveling a length $\propto l_m^2/W$ along the wire direction to enclose the same geometrical area. The AB phase arises from a magnetic vector potential $\vec{A}$. A mapping exists from Rashba SOI to the physics arising from an effective vector potential[28] involving $\vec{E}$, the actual or effective electric field at the origin of SOI by breaking inversion
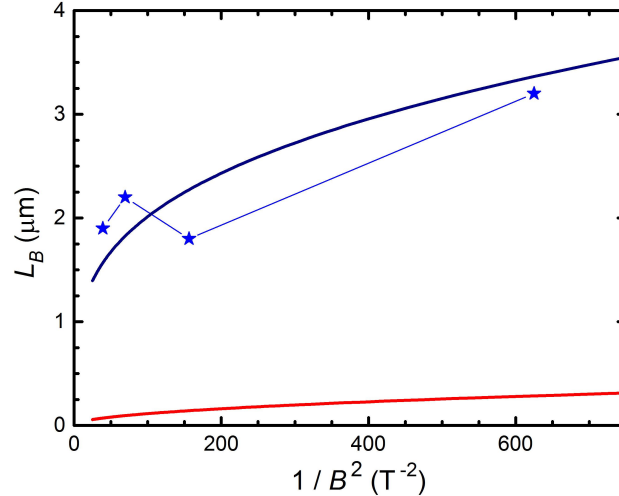
Figure 4: Experimental values for L_B plotted *vs* $1/B^2$ to emphasize the expected dependence of L_B on B (blue symbols). The upper navy-colored solid line represents the expression for L_B mentioned in the text. The lower red solid line represents $L_B = \sqrt{3}\, l_m^2/W$, which does not fit the data. The respective fits show that despite scatter in the data, the experiment[17] succeeds in differentiating between models for L_B.

symmetry (in duality to B breaking time-reversal symmetry). This so-called Aharonov-Casher vector potential[29,30] is $\vec{A_{ac}} = (1/c^{*2})\vec{\mu} \times \vec{E}$, where $\vec{\mu}$ is the particle's magnetic moment and c^* the effective velocity of light (a bandstructure parameter[31]). It can be shown that under SOI L_Ω takes the role assumed in B by l_m, providing an equivalent geometrical phase relation. Within prefactors of order unity dependent on boundary conditions, the geometrical phase argument that yielded $L_B \propto l_m^2/w$ now yields $L_S \propto L_\Omega^2/W$. We note that if SOI is weak, then $L_S \to \infty$ and the only length scale entering Eq. (1) is $\left(L_\phi^{-2} + L_B^{-2}\right)^{-\frac{1}{2}}$. The role of L_B in this expression was confirmed experimentally in previous work[17] performed using the high-mobility $In_{0.64}Ga_{0.36}As/In_{0.45}Al_{0.55}As$ heterostructure. The sample geometry was a 5x5 interferometric ring array operating in a Sagnac-like mode, which emphasizes the contribution of time-reversed paths. The measurement geometry was thus sensitive to time-reversal symmetry breaking, and indeed confirmed the phase-breaking role of L_B. Quantitative results (Fig. 4) showed that the expression $L_B = l_m\sqrt{C_1 l_m^2 \ell_e/W^3 + C_2 \ell_e^2/W^2}$ fit the data obtained for $L_B(B)$ best, as expected for a ballistic confined system over a wider range of B. It is hence concluded that geometrical quantum phases, illustrated here by the AB phase and its electromagnetic dual, the Aharonov-Casher phase, lead to quantifiable dephasing effects in quantum transport via effective lengths, L_B and L_S *resp*. The quantifiable aspect further leads us to conclude that other geometrical phases, *e.g.* Berry's phases[32] arising from the kinematics of a system, can likewise be accessed using this mesoscopic quantum transport approach.

5. ANALYSIS OF EFFECTS DUE TO DEVICE GEOMETRY

Values for L_ϕ in wires (Fig. 1) fabricated on the $In_{0.53}Ga_{0.47}As/In_{0.52}Al_{0.48}As$ heterostructure show a positive correlation with the wire length L. Figure 5 depicts L_ϕ (obtained at $T = 0.38$ K) *vs* a
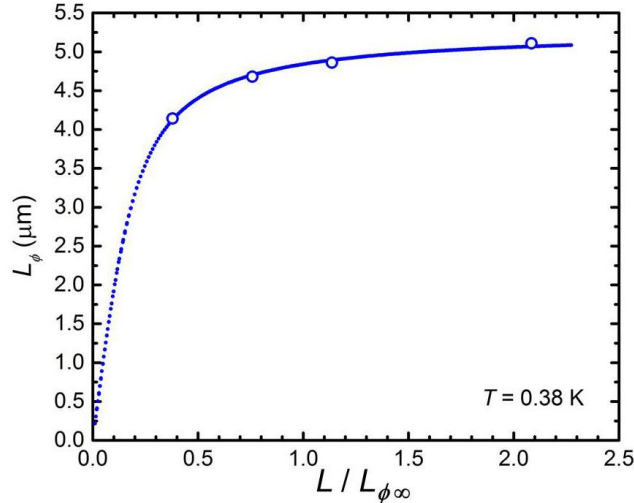
Figure 5: L_ϕ vs $L/L_{\phi\infty}$, in wires of length L at $T = 0.38$ K. Open circles represent data, and the dashed line represents a fit to the expression mentioned in the text, with $L_{\phi\infty} = 5.3$ µm.

normalized value for L in wires with $L= 2.0$ µm, 4.0 µm, 6.0 µm and 11.0 µm. An increase in L yields an increase in L_ϕ, with L_ϕ tending asymptotically to a value $L_{\phi\infty}$ for long L. The result of Fig. 5 can be explained by decoherence via interaction of electrons at the wire endpoints with the wider classical environment, named environmental coupling decoherence.[5–7] In longer wires the interaction at the endpoints is relatively less important wires due to averaging of the measured L_ϕ over the wire. Hence longer wires show longer L_ϕ tending towards an asymptotic value $L_{\phi\infty}$ as observed. In Fig. 5 we find $L_{\phi\infty} = 5.3$ µm. $L_{\phi\infty}$ was obtained using a fit (depicted in Fig. 5) to the expression[8,33] $L_\phi = L_{\phi\infty}(\coth\left(\frac{L}{L_{\phi\infty}}\right) - \frac{L_{\phi\infty}}{L})$, derived for the amplitude of quantum-coherent backscattering for a diffusing electron assuming perfectly transparent contacts at the wire endpoints.

In contrast to simple wires, values for L_ϕ in stadia with side-wires (Fig. 1) fabricated on the $In_{0.53}Ga_{0.47}As/In_{0.52}Al_{0.48}As$ heterostructure show a more intricate dependence on the side-wire W and L. The samples featured stadia with a common inner diameter 4.0 µm, but with varying side-wire dimensions: $W = 1.4$ µm and $L = 1.0$ µm ($W/L = 1.4$); $W = 1.0$ µm and $L = 1.0$ µm ($W/L = 1.0$); $W = 1.0$ µm and $L = 3.0$ µm ($W/L = 0.33$); $W = 0.6$ µm and $L = 1.0$ µm ($W/L = 0.6$). Figure 6 depicts L_ϕ (obtained at $T = 0.38$ K) vs W/L in the stadia. Environmental coupling decoherence predicts that the wider or shorter the side wire is, the shorter L_ϕ is, and hence cannot explain the observed dependence of L_ϕ on W/L. The results can be explained by the composite nature of the samples, namely by stadium-wire coupling decoherence. Device-device (here stadium-wire) coupling decoherence finds its origin in low wavefunction hybridization between different geometries. We express the total decoherence rate as $\frac{1}{\tau_\phi} = \frac{1}{\tau_{\phi 0}} + \frac{1}{\tau_d} + 2\gamma_\alpha$ where γ_α denotes the stadium-wire coupling decoherence rate with the factor 2 originating in 2 connection points. The second term denotes environmental interaction decoherence via τ_d.[7,34] Between identical quantum dots in arrays,[5,35] a low *dot-dot* coupling decoherence rate γ_α was deduced due to the identical geometries of the interacting quantum dots. In stadium-wire coupling, γ_α is similarly dependent on any geometrical similarity between the circular stadia and the side-wires. In the data of Fig. 6, the effects of γ_α are sufficiently large to be observed, dominating over $1/\tau_d$ due to

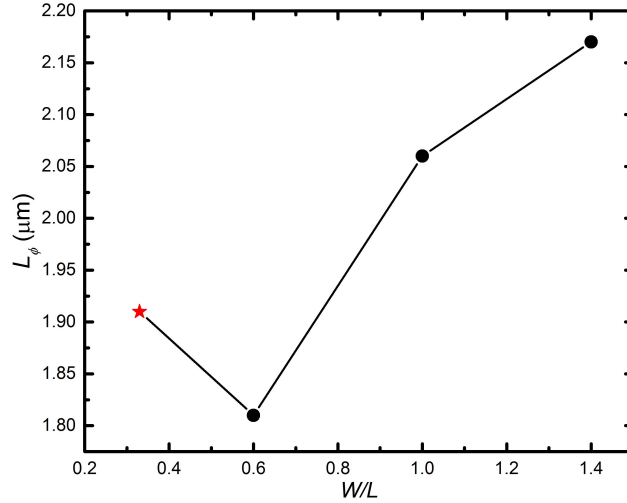Figure 6: L_ϕ vs W/L, in stadia of with side-wires of width W and length L, at $T = 0.38$ K. Symbols represent data, and the solid line function as guide only. The datapoint represented by a red star is explained in the text.

the difference in geometry between stadia and side-wires. W and L of side-wires are comparable to the 2 µm radius of the stadia and hence stronger geometrical similarity with the stadia and the side-wires can be quantified by W/L with a lower W/L denoting stronger geometrical similarity. For the samples with $W/L > 0.33$, increasing W/L by either wider W or shorter L, increases wavefunction hybridization and hence increases L_ϕ, as shown in Fig. 6. For the sample with $W/L = 0.33$ the side-wire with long $L = 3$ µm dominates the results, and environmental interaction decoherence partially masks the effect of stadium-wire coupling decoherence.

Apart from the effects of geometrical phases, the above examples show that sample geometry, including internal layout of the device and its interaction with a classical wider environment, plays an important role in determining measured values for L_ϕ.

6. CONCLUSIONS

The dependence of the quantum phase coherence length L_ϕ on geometrical phases and on device geometry is described, starting from experimental observations. An analysis of the dependence of L_ϕ on the phase space allowed for geometrical phases to develop yields insight in and a quantification of geometrical phases, which play an important role in quantum physics. Interaction with a classical environment is shown to limit quantum coherence in short wires, leading to a decreasing L_ϕ in shorter wires. For stadia, experiments show that internal stadium-wire coupling decoherence can dominate over environmental coupling decoherence effects.

ACKNOWLEDGMENTS

REFERENCES

[1] B. Hackens, F. Delfosse, S. Faniel, C. Gustin, H. Boutry, X. Wallart, S. Bollaert, A. Cappy, and V. Bayot. Long dephasing time and high-temperature conductance fluctuations in an open InGaAs quantum dot. *Phys. Rev. B*, 66:241305(R), 2002.

[2] J. J. Lin and J. P. Bird. Recent experimental studies of electron dephasing in metal and semiconductor mesoscopic structures. *J. Phys.: Condens. Matter*, 14:R501, 2002.

[3] M. Ferrier and L. Angers and A. C. H. Rowe and S. Guéron and H. Bouchiat and C. Texier and G. Montambaux and D. Mailly. Direct measurement of the phase-coherence length in a GaAs/GaAlAs square network. *Phys. Rev. Lett.*, 93:246804, 2004.

[4] S. L. Ren, J. J. Heremans, C. K. Gaspe, S. Vijeyaragunathan, T. D. Mishima, and M. B. Santos. Aharonov-Bohm oscillations, quantum decoherence and amplitude modulation in mesoscopic InGaAs/InAlAs rings. *J. Phys.: Condens. Matter*, 25:435301, 2013.

[5] M. Elhassan, J. P. Bird, R. Akis, D. K. Ferry, T. Ida, and K. Ishibashi. Dephasing due to coupling to the external environment in open quantum-dot arrays. *J. Phys.: Condens. Matter*, 17:L351, 2005.

[6] J. P. Bird, A. P. Micolich, D. K. Ferry, R. Akis, Y. Ochiai, Y. Aoyagi, and T. Sugano. The influence of environmental coupling on phase breaking in open quantum dots. *Solid-State Electron.*, 42:1281, 1998.

[7] B. Hackens, S. Faniel, C. Gustin, X. Wallart, S. Bollaert, A. Cappy, and V. Bayot. Dwell-time-limited coherence in open quantum dots. *Phys. Rev. Lett.*, 94:146802, 2005.

[8] E. Akkermans and G. Montambaux. *Mesoscopic physics of electrons and photons*. Cambridge, 2007.

[9] R. L. Kallaher, J. J. Heremans, N. Goel, S. J. Chung, and M. B. Santos. Spin and phase coherence lengths in n-InSb quasi-one-dimensional wires. *Phys. Rev. B*, 81:035335, 2010.

[10] R. L. Kallaher, J. J. Heremans, W. Van Roy, and G. Borghs. Spin and phase coherence lengths in InAs wires with diffusive boundary scattering. *Phys. Rev. B*, 88:205407, 2013.

[11] S. V. Iordanskii, Y. B. Lyanda-Geller, and G. E. Pikus. Weak localization in quantum wells with spin-orbit interaction. *Pis'ma Zh. Eksp. Teor. Fiz*, 60:199, 1994) (JETP Lett. 60, 206(1994)).

[12] G. Bergmann. Weak localization and its applications as an experimental tool. *Int. J. Mod. Phys. B*, 24:2015, 2010.

[13] V. Deo, Y. Zhang, V. Soghomonian, and J. J. Heremans. Quantum interference measurement of spin interactions in a bio-organic/semiconductor device structure. *Sci. Rep.*, 5:9487, 2015.

[14] R. A. Jalabert, H. U. Baranger, and A. D. Stone. Conductance fluctuations in the ballistic regime: A probe of quantum chaos? *Phys. Rev. Lett.*, 65:2442, 1990.

[15] D. K. Ferry, R. A. Akis, D. P. Pivin Jr, J. P. Bird, and N. Holmberg. Quantum transport in ballistic quantum dots. *Phys. E*, 3:137, 1998.

[16] M. Rudolph and J. J. Heremans. Spin-orbit interaction and phase coherence in lithographically defined bismuth wires. *Phys. Rev. B*, 83:205410, 2011.

[17] S. L. Ren, J. J. Heremans, S. Vijeyaragunathan, T. D. Mishima, and M. B. Santos. Determination of time-reversal symmetry breaking lengths in an InGaAs interferometer array. *J. Phys.: Condens. Matter*, 27:185801, 2015.

[18] M. Rudolph and J. J. Heremans. Electronic and quantum phase coherence properties of bismuth thin films. *Appl. Phys. Lett.*, 100:241601, 2012.

[19] R. L. Kallaher, J. J. Heremans, N. Goel, S. J. Chung, and M. B. Santos. Spin-orbit interaction determined by antilocalization in an InSb quantum well. *Phys. Rev. B*, 81:075303, 2010.

[20] Yao Zhang and J. J. Heremans. Effects of ferromagnetic nanopillars on spin coherence in an InGaAs quantum well. *Solid State Comm.*, 177:36, 2014.

[21] P. Hofmann. The surfaces of bismuth: Structural and electronic properties. *Prog. Surf. Sci.*, 81:191, 2006.

[22] J. J. Heremans, R. L. Kallaher, M. Rudolph, M. Santos, W. Van Roy, and G. Borghs. Spin-orbit interaction and spin coherence in narrow-gap semiconductor and semimetal wires. *Proc. of SPIE*, 9167:91670D, 2014.

[23] A. Zduniak, M. I. Dyakonov, and W. Knap. Universal behavior of magnetoconductance due to weak localization in two dimensions. *Phys. Rev. B*, 56:1996, 1997.

[24] C. W. J. Beenakker and H. van Houten. Boundary scattering and weak localization of electrons in a magnetic field. *Phys. Rev. B*, 38:3232, 1988.

[25] R.Winkler. *Spin-Orbit Coupling Effects in Two-Dimensional Electron and Hole Systems*. Springer Tracts in Modern Physics 191, 2003.

[26] S. Kettemann. Dimensional control of antilocalization and spin relaxation in quantum wires. *Phys. Rev. Lett.*, 98:176808, 2007.

[27] A. G. Aronov and Yu. V. Sharvin. Magnetic flux effects in disordered conductors. *Rev. Mod. Phys.*, 59:755, 1987.

[28] S. G. Tan T. Fujita, M. B. A. Jalil and S. Murakami. Gauge fields in spintronics. *J. Appl. Phys.*, 110:121301, 2011.

[29] Y. Aharonov and A. Casher. Topological quantum effects for neutral particles. *Phys. Rev. Lett.*, 53:319, 1984.

[30] S. Ren L. L. Xu and J. J. Heremans. Magnetoelectronics at edges in semiconductor structures: helical aharonov-casher edge states. *Integr. Ferroelectr.*, 131:36, 2011.

[31] W. Zawadzki. Zitterbewegung and its effects on electrons in semiconductors. *Phys. Rev. B*, 72:085217, 2005.

[32] M.-C. Chang Di Xiao and Qian Niu. Berry phase effects on electronic properties. *Rev. Mod. Phys.*, 82:1959, 2010.

[33] B. Doucot and R. Rammal. Interference effects and magnetoresistance oscillations in normal-metal networks:1-weak localization approach. *J. Physique*, 47:973, 1986.

[34] B. Hackens, S. Faniel, C. Gustin, X. Wallart, S. Bollaert, A. Cappy, and V. Bayot. Dwell-time related saturation of phase coherence in ballistic quantum dots. *Physica E*, 34:511, 2006.

[35] M. Elhassan, J. P. Bird, A. Shailos, C. Prasad, R. Akis, D. K. Ferry, Y. Takagaki, L.-H. Lin, N. Aoki, Y. Ochiai, K. Ishibashi, and Y. Aoyagi. Coupling-driven transition from multiple to single-dot interference in open quantum-dot arrays. *Phys. Rev. B*, 64:085325, 2001.

Jean J. Heremans is professor of Physics at Virginia Tech. He received his MS and PhD degrees from Princeton University. His current research interests include spin physics in the solid-state, spin-orbit interaction, quantum coherence, and quantum transport.

Biographies and photographs of the other authors are not available.

List of Figures